



Rationally constructing a 3D bifunctional solar evaporator for high-performance water evaporation coupled with pollutants degradation

Lingfang Cui^a, Chenwei Ma^a, Peifang Wang^a, Huinan Che^a, Haolan Xu^{b,*}, Yanhui Ao^{a,*}

^a Key Laboratory of Integrated Regulation and Resource Development on Shallow Lakes, Ministry of Education, College of Environment, Hohai University, No.1, Xikang Road, Nanjing 210098, China

^b Future Industries Institute, UniSA STEM, University of South Australia, Mawson Lakes Campus, Adelaide, SA 5095, Australia

ARTICLE INFO

Keywords:

Interfacial solar evaporation
Photothermal materials
Pollutant degradation
Peroxymonosulfate
Confinement
Van der Waals interaction

ABSTRACT

In this work, nitrogen-doped carbon nanotubes encapsulated with Co are grown on carbon fibers (Co-NCNT/CF) and utilized as photothermal materials to construct 3D evaporators, which simultaneously realize highly efficient solar evaporation and organic pollutant degradation. The deliberate structure enables the 3D evaporator to take advantage of the spontaneously generated internal convection flow to significantly enhance solar evaporation, achieving a high evaporation rate of $3.85 \text{ kg m}^{-2} \text{ h}^{-1}$ under 1.0 sun irradiation. More importantly, the evaporator exhibits excellent performance on peroxymonosulfate (PMS) activation, effectively preventing phenol in water sources from entering the condensed clean water. Density functional theory (DFT) calculation shows that the enhanced van der Waals interaction facilitates PMS adsorption and activation on the confined inner surfaces of Co-NCNT compared to the unconfined system. This solar evaporator successfully combines interfacial solar evaporation and advanced oxidation processes, providing a new strategy for producing clean water from water sources containing organic volatiles.

1. Introduction

Solar-driven interfacial evaporation is a very promising technology for producing clean water from seawater and wastewater using solar energy [1–5]. Typically, interfacial evaporation over two-dimensional (2D) materials/evaporators occurs at air-water interfaces [6–8]. However, the evaporation fluxes of 2D evaporators are relatively low and the energy conversion efficiency from solar energy to vapor can hardly exceed the theoretical limit [9–11]. To break the theoretical limit, three-dimensional (3D) evaporators were designed and fabricated [3, 12–18]. In this regard, reasonable 3D structural design can enlarge total evaporation surface area, harvest extra energy from the environment and take advantage of external convection to enhance the overall evaporation rate beyond the theoretical limit [14,19,20], which showed great potential in practical applications. However, developing advanced 3D evaporators to further explore new strategies to improve evaporation rate and new functions to treat a wide range of water sources is still highly required.

During interfacial solar evaporation processes, some organic pollutants in water especially the volatile organic compounds (VOC) will also evaporate and contaminate the condensed clean water [21]. To

solve this problem, in principle, the VOC in the water sources must be degraded before being evaporated. It was found that coupling solar-driven interfacial evaporation with photodegradation can efficiently remove VOC from water [1,22–27]. At present, the advanced oxidation process based on peroxymonosulfate (PMS) can generate various reactive oxygen species (ROS), such as hydroxyl ($\bullet\text{OH}$), sulfate ($\text{SO}_4^{\bullet-}$), superoxide radicals ($\bullet\text{O}_2$) and nonradicals such as singlet oxygen ($^1\text{O}_2$) [1,28–30]. During interfacial solar evaporation, the sufficient light, high air-water interfacial temperature, carbon-based and transition metal photothermal materials all provide required conditions for activation of PMS [1,31–33]. Therefore, introducing and activating PMS in an interfacial solar evaporation system should be able to simultaneously achieve efficient solar evaporation and catalytic degradation of VOCs, killing two birds with one stone. To realize this, designing and fabricating bifunctional photothermal materials and solar evaporators is the key [34,35].

Based on the above considerations, herein, a novel Co-NCNT/CF-based 3D solar evaporator was designed (Scheme 1a). In this system, carbon nanotube (CNT) arrays were directly grown on the carbon fibers (CFs) and utilized as both photothermal material and catalyst. The 3D evaporator was designed to be with a specified height (i.e., side

* Corresponding authors.

E-mail addresses: haolan.xu@unisa.edu.au (H. Xu), andyao@hhu.edu.cn (Y. Ao).

<https://doi.org/10.1016/j.apcatb.2023.122988>

Received 28 March 2023; Received in revised form 23 May 2023; Accepted 9 June 2023

Available online 12 June 2023

0926-3373/© 2023 Elsevier B.V. All rights reserved.

evaporation surface), which ensured a larger evaporation area and enabled effective extra energy harvest from the environment (Scheme 1b). Furthermore, for the first time, due to the porous structure of the evaporation surface (i.e., Co-NCNT/CF) and the elaborately designed hollow frame-like evaporator support, the 3D evaporator could take advantage of the spontaneously generated convection inside the evaporator to facilitate vapor escape, significantly enhancing solar evaporation (Scheme 1c). In addition, density functional theory (DFT) calculation showed that the enhanced van der Waals interactions facilitated PMS adsorption and activation on the confined inner surface of Co-NCNT compared to the unconfined system. As a result, Co-NCNT/CF could generate abundant active sites for PMS activation and boost VOC removal during interfacial solar evaporation.

2. Results and discussion

2.1. Characterization of Co-NCNT/CF evaporator

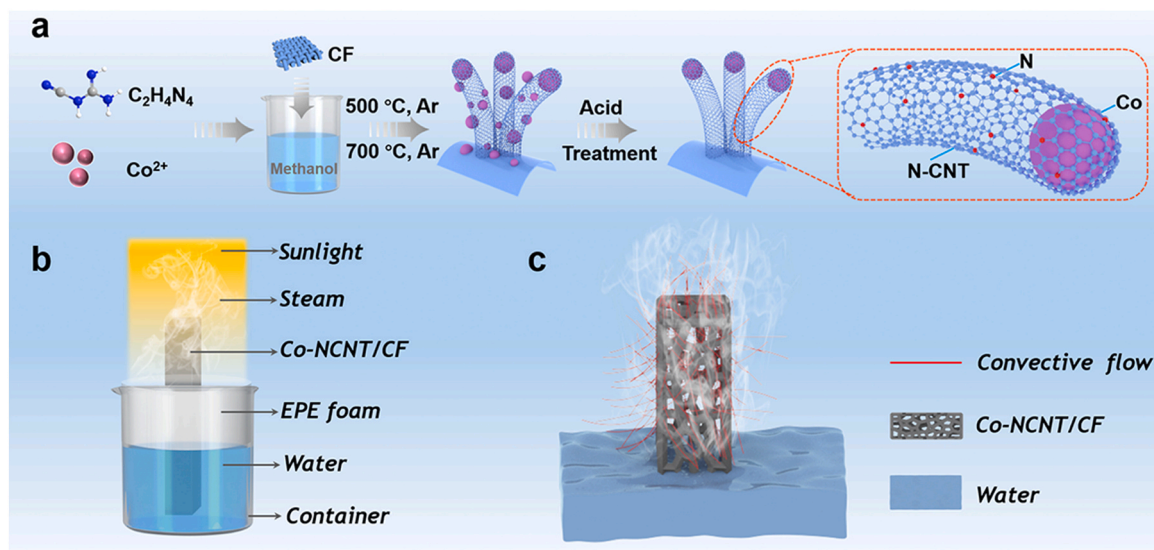
In this work, nitrogen-doped carbon nanotubes (NCNTs) were grown on carbon fibers (CF) via the catalysis of trapped Co (Co-NCNT/CF) (Scheme 1a). XRD patterns (Fig. 1a) exhibited a sharp and strong diffraction peak at 25.6° , which corresponded to the (002) plane of graphitic carbon [36,37]. Compared with the XRD pattern of NCNT/CF, the diffraction peaks at 44.2° in Co-NCNT/CF assigned to metallic Co, indicating that metallic Co was not removed after acid treatment owing to the protection from carbon nanoshells [38]. Generally, Co nanoparticles (Co NPs) play a catalytic role in the growth of CNTs [39]. White dots at the tips of CNTs could be observed in the SEM image of Co-NCNT/CF (Fig. 1b), indicating the successful incorporation of Co-NPs. As expected, TEM image clearly revealed that Co-NCNT/CF was composed of folded bamboo-like CNTs and wrapped Co NPs (Fig. 1c). The hollow bamboo-like structure and raised folds are beneficial to light capture and water permeability, providing sufficient space for transportation and diffusion of water and vapor, and improving the light absorption efficiency. In addition, doping nitrogen and embedding Co NPs can inject electrons into the nearby carbon layer, thereby improving the catalytic activity of Co-NCNT/CF. The carbon layer blocks the direct contact between Co NPs and the external reaction environment, which is conducive to the stability of Co-NCNT/CF [40]. Energy dispersive X-ray spectroscopy (EDS) (Fig. S1) showed that Co, N and C were distributed in the Co-NCNT/CF, where SEM and TEM images confirmed that NCNT/CF was successfully prepared (Fig. S2). As shown in Fig. 1d, the

peak intensity ratio I_D/I_G from Raman spectrum suggested that Co-NCNT/CF had an improved degree of graphitization. The presence of the 2D-band further pointed to the formation of the CNT structures [40, 41]. More information can be garnered from X-ray photoelectron spectroscopy (XPS) analysis. Other than the pronounced C, N and O elements, the XPS survey spectra (Fig. S3a) of Co-NCNT/CF showed an additional feature of Co species. For Co 2p spectrum (Fig. 1e), the peaks located at around 782.3, 780.7, and 779.1 eV were assigned to Co^{3+} , Co^{2+} and Co^0 , respectively [42]. The N 1s signal in Fig. 1f of the samples could be deconvoluted into 398.3, 400.1 and 401.3 eV assigned to pyridinic N, pyrrolic N and graphitic N, respectively. However, one additional peak at 399.1 eV presented in Co-NCNT/CF could be attributed to Co-N [43,44]. The pore structures of NCNT and Co-NCNT were analyzed by nitrogen adsorption/desorption at 77 K (Fig. S4). For NCNT, the specific surface area and pore volume are $80.91 \text{ m}^2 \text{ g}^{-1}$ and $0.24 \text{ cm}^3 \text{ g}^{-1}$, respectively. The specific surface area of Co-NCNT is $110.15 \text{ m}^2 \text{ g}^{-1}$ with a pore volume of $0.42 \text{ cm}^3 \text{ g}^{-1}$. The pore size of NCNT and Co-NCNT were 9.96 and 27.90 nm, respectively. The large specific surface area can expose more active sites to enhance catalytic activity, and rich pore structure are conducive to the transmission and diffusion of molecules.

Evaluating light-to-heat conversion capability of the evaporators is an essential requirement for interfacial solar evaporation. The dynamic temperature of the prepared evaporators under intermittent light irradiation was recorded and shown in Fig. 1g-h. Upon light irradiation, the surface temperature of the Co-NCNT/CF evaporator increased to $\sim 53^\circ \text{C}$ in a short time within 450 s, while the temperature of NCNT/CF could merely reach up to $\sim 46^\circ \text{C}$ at the same time interval. As shown in Fig. 1i and Fig. S5, compared to pure CF and NCNT/CF, the Co-NCNT/CF exhibited broad light absorption from 250 to 2500 nm, which covered the entire solar spectrum range. Accordingly, the absorption of Co-NCNT/CF, NCNT/CF and CF at 300–2500 nm is 91.55%, 89.91% and 81.12%, respectively. The strong light absorption should be ascribed to the unique structure of Co-CNT, which provided a large number of optical micro-cavities and introduced the plasmonic effect of Co NPs [45, 46]. In addition, water contact angle measurement confirmed the excellent hydrophilicity of the Co-NCNT/CF (Fig. S7), which will benefit the water supply during interfacial solar evaporation.

2.2. Investigation on the effect of convection on evaporation

Encouraged by the outstanding light-to-heat conversion capability of



Scheme 1. (a) Scheme of the fabrication of Co-NCNT/CF. (b) Experimental setup for solar evaporation using the Co-NCNT/CF-based evaporator. (c) Schematic illustration of the spontaneously generated convection inside the Co-NCNT/CF evaporator (cross-sectional view) for enhancing solar evaporation.

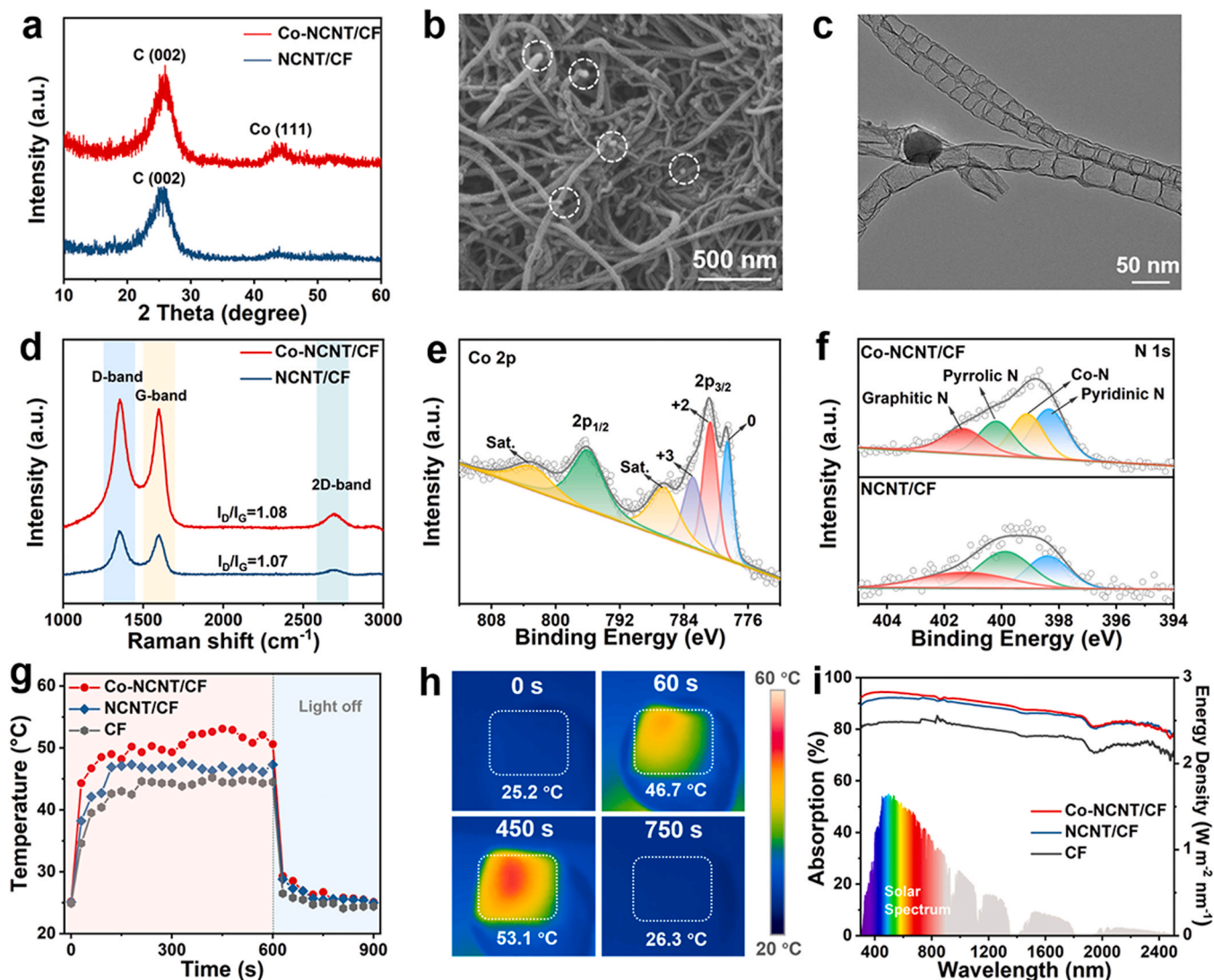


Fig. 1. (a) XRD patterns of the Co-NCNT/CF and NCNT/CF. (b) SEM image of the Co-NCNT/CF. (c) TEM image of Co-NCNT indicating that a Co NP is embedded in the CNTs. (d) Raman spectra of the as-prepared Co-NCNT/CF and NCNT/CF. The high-resolution XPS of the (e) Co 2p spectrum and (f) N 1s spectra. (g) Surface temperature curves of the Co-NCNT/CF and NCNT/CF, and (h) infrared images of Co-NCNT/CF evaporator under 1 sun irradiation. (i) UV-Vis-NIR spectra of CF, NCNT/CF and Co-NCNT/CF evaporator.

Co-NCNT/CF, interfacial solar vapor generation performance was investigated. The evaporator was composed of a photothermal layer (Co-NCNT/CF), an evaporator support, an expandable polyethylene (EPE)

foam and bulk water (Scheme 1a). The evaporator support was made of a hollow nickel foam frame (denoted as Ni-F-Co-NCNT/CF) or enclosed nickel foam tube with different pore sizes of 0.2, 1, and 3 mm (denoted

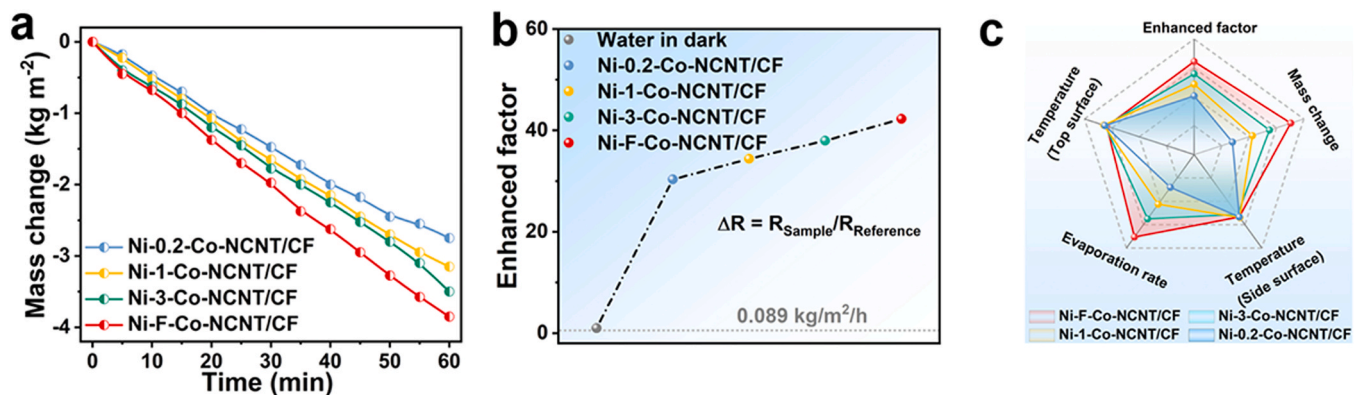


Fig. 2. (a) Water mass change using nickel foam hollow frame and nickel foam tubes with different pore sizes as the evaporator support under 1.0 sun irradiation. (b) The enhancement factor of evaporation rate (i.e., ΔR). (c) Qualitative comparisons of solar-driven evaporation performance of the four systems by a radar chart.

as Ni-0.2-Co-NCNT/CF, Ni-1-Co-NCNT/CF, and Ni-3-Co-NCNT/CF), respectively (Fig. S7a). The evaporator support was designed to a specified height, which ensured a larger side evaporation surface area and enabled it to effectively harvest energy from the environment (Fig. S7b). Under 1.0 sun irradiation, it was clearly observed that the Ni-F-Co-NCNT/CF evaporator delivered the highest evaporation rate of $3.85 \text{ kg m}^{-2} \text{ h}^{-1}$ (Fig. 2a, Fig. S8). Compared with the natural evaporation of water, the Ni-F-Co-NCNT/CF evaporation system displayed a dramatic enhancement in evaporation performance by ~ 42 times (Fig. 2b). By comparison, the Ni-F-Co-NCNT/CF evaporator demonstrated obvious advantages over other evaporators (Fig. 2c). The Ni-F-Co-NCNT/CF evaporator can timely remove the vapor generated on the side surface by the spontaneously generated air convection inside the evaporator since the used nickel foam frame didn't block the internal airflow, thus improving the evaporation rate. For the evaporators using nickel foam tube supports, the evaporation rate gradually decreased with the decrease in pore size of the nickel foam (3.5, 3.15 and $2.75 \text{ kg m}^{-2} \text{ h}^{-1}$ for Ni-3-Co-NCNT/CF, Ni-1-Co-NCNT/CF, and Ni-0.2-Co-NCNT/CF, respectively), since the enclosed evaporator support and small pores prevented the internal air convection from reaching the evaporation surfaces [47,48]. In addition, by monitoring the evaporation surface temperature using an IR camera during solar evaporation (Fig. S9), it could be verified that the evaporator harvested extra energy from the environment. Under 1.0 sun irradiation, the temperatures of

the top surfaces reached at 31.9, 32.5, 33 and 32.6°C , respectively. Notably, the temperature of the top surface of the Ni-F-Co-NCNT/CF evaporator was the lowest, indicating the lowest energy loss to the environment by radiation and convection [3,49]. And the lowest top surface temperature promotes heat transfer from the top evaporation surface to the side evaporation surfaces, reducing heat accumulation on the top surface. While, simultaneously the side surfaces not receiving light underwent. Meanwhile, cold evaporation occurs on the side surfaces that do not receive light due to the cooling effect of water evaporation, and the side surface temperature is lower than the ambient temperature. Therefore, under solar irradiation, the side surfaces can obtain energy from the environment. The energy analysis of the Ni-F-Co-NCNT/CF evaporation system during solar vapor generation is presented in Note S8. The calculated q_{recycle} was 0.5 W, which was even higher than the solar light energy input ($P_{\text{light}}=0.388 \text{ W}$). Therefore, the Ni-F-Co-NCNT/CF evaporation system could draw massive extra energy from the environment.

In light of the above facts, it is considered that the specifically designed 3D evaporator can effectively take advantage of internal convection flow to enhance solar evaporation. To further verify the existence of internal convection and its positive effect on solar evaporation, COMSOL Multiphysics was employed to simulate the convective flow generated by the 3D evaporators during interfacial solar evaporation. The simulation modelling geometries and boundary conditions are

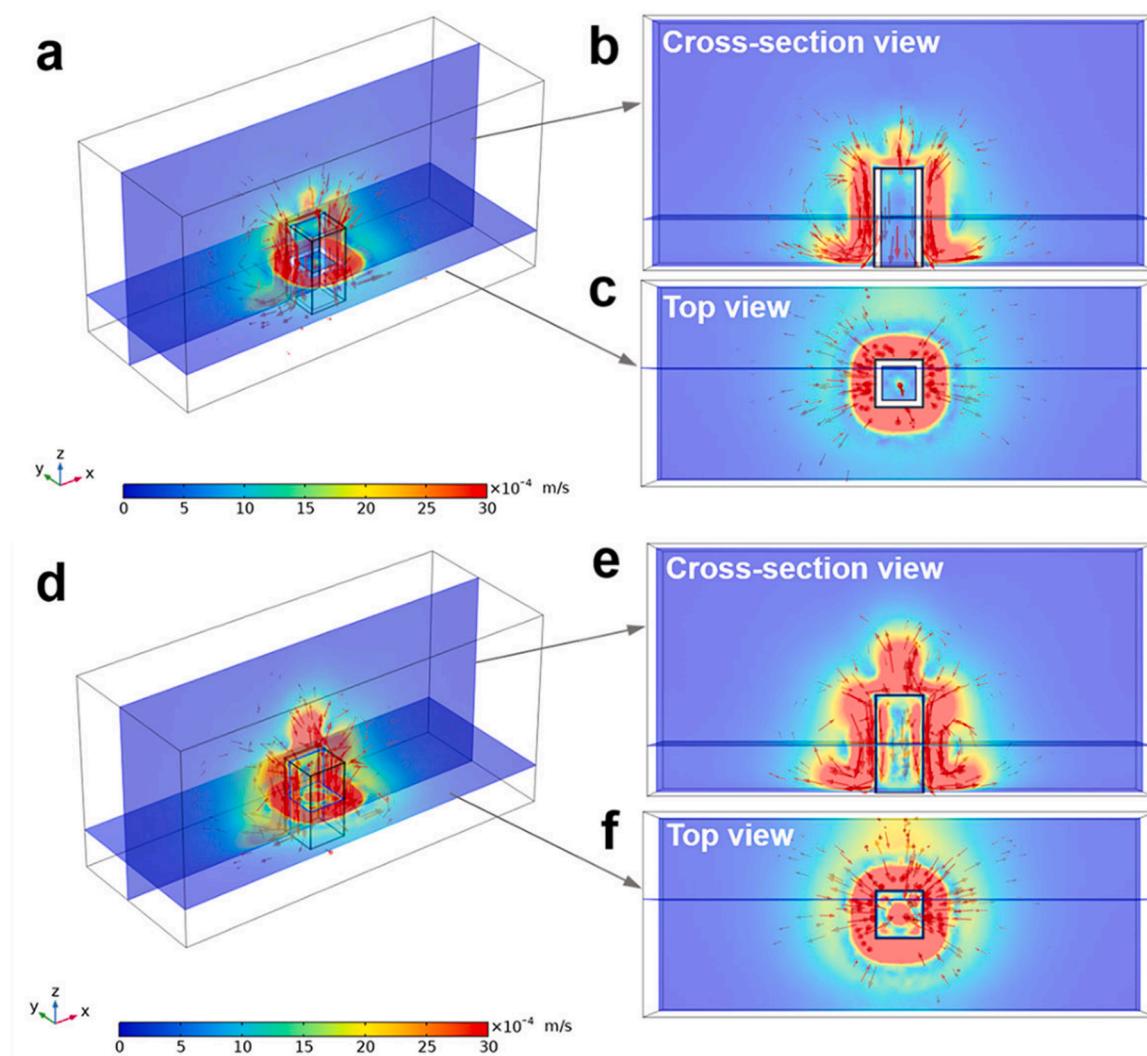


Fig. 3. Simulated spontaneously generated internal and external convection flow around the evaporator during solar evaporation. (a) Ni-0.2-Co-NCNT/CF evaporation system and its (b) cross-section view and (c) top view. (d) Ni-F-Co-NCNT/CF evaporation system and its (e) cross-section view and (f) top view.

presented in Fig. S10. As shown in Fig. 3, during solar evaporation, convection flow was spontaneously formed both inside and outside the evaporator due to the temperature difference between the top and side evaporation surfaces. The formed convection should be conducive to the rapid escape of the generated vapor. However, ascribed to the presence of enclosed evaporator support in Ni-0.2-Co-NCNT/CF evaporator, the internal and external convection was isolated, and the internal convection has little contribution to the vapor escape on the evaporation surfaces (Fig. 3a-c). However, for the Ni-F-Co-NCNT/CF evaporator with a hollow frame evaporator support, the cross-section and top views showed that convection could flow through the top and side surfaces of the evaporator, thus the internal convection could effectively push the generated vapor away from the side evaporation surfaces, facilitating continuous efficient water evaporation (Fig. 3d-f). Therefore, Ni-F-Co-NCNT/CF evaporator was able to not only harvest energy from the environment but also make use of the spontaneously generated internal convection flow to maximize the evaporation rate. The Ni-F-Co-NCNT/CF evaporator with the best evaporation performance was employed in further study.

The height of the Ni-F-Co-NCNT/CF evaporator (i.e., the exposed side evaporation area) affects the energy harvest from the environment. The evaporation rate increased significantly with the increase in height

from 0 to 2, 4 and 6 cm (Fig. S11-S12). It is found that the temperature of the top surface decreases significantly as the height increases from 0 to 2, 4 and 6 cm. Furthermore, the internal convection also affected the evaporation on the top surface depending on the design of the evaporation support. After adding a Ni foam cap on the top of the Ni frame evaporator support (i.e., below the top evaporation surface) (Fig. S13), the evaporation rate decreased to $3.35 \text{ kg m}^{-2} \text{ h}^{-1}$, which was $\sim 13\%$ lower than that of the evaporator without Ni foam cap. The decrease in evaporation rate was due to the blocked air convection near the backside of the top evaporation surface by the nickel foam cap. In this case, the convection flow inside the evaporator could not contribute to the vapor removal on the top evaporation surface (Fig. S14). As a result, for the Ni-F-Co-NCNT/CF evaporation system with Ni foam cap, the thermal energy was not efficiently consumed by water evaporation on the top surface, resulting in a higher evaporation surface temperature of 36.2°C (Fig. S15).

2.3. Simultaneous solar evaporation and PMS mediating water purification

Considering that many water sources contain organic pollutants such as VOCs, the use of a normal solar evaporator cannot reliably lead to

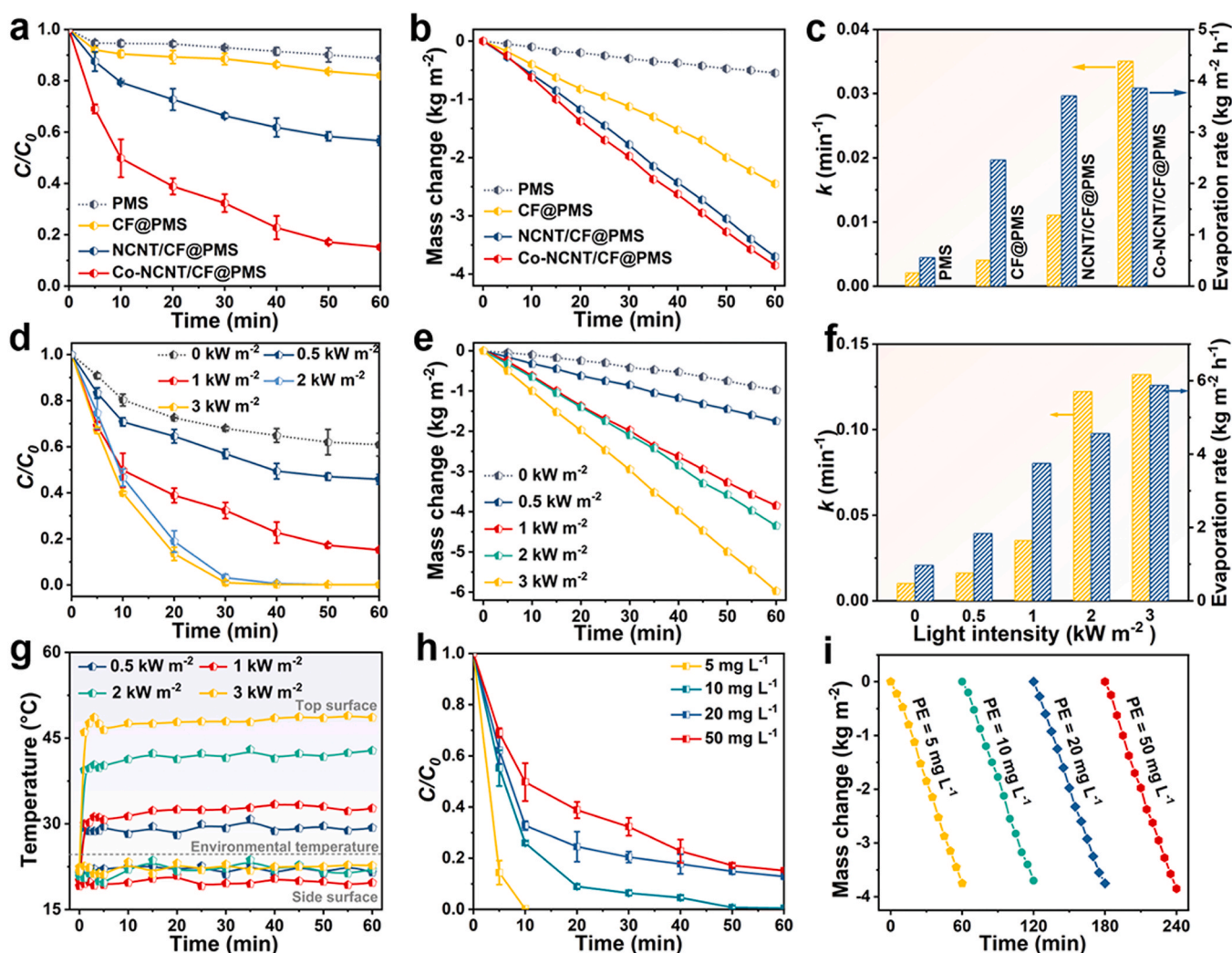


Fig. 4. (a) The PE degradation efficiencies, (b) water mass change curves, (c) rate constant and evaporation rate in different system under 1 sun irradiation. (Reaction condition: [PE] = 50 mg L^{-1} , [PMS] = 2 mM). (d) The PE degradation efficiencies, (e) water mass change curves, (f) rate constant and evaporation rate, (g) time-dependent top and side evaporation surface temperature change of Co-NCNT/CF evaporator under different light intensities. (Reaction condition: [PE] = 50 mg L^{-1} , [PMS] = 2 mM). (h) The PE degradation efficiencies and (i) water mass change curves of Co-NCNT/CF evaporator with different PE concentrations under 1 sun irradiation.

clean water production. However, the advanced oxidation technology based on PMS has shown excellent performance in organic pollutant removal. Inspired by this, the Ni-F-Co-NCNT/CF evaporation system was further upgraded for simultaneous PMS-mediated water purification and solar evaporation. 50 mg L⁻¹ of PE was chosen as the target pollutant. During dark evaporation, in the presence of PMS, the removal efficiencies of PE by Co-NCNT/CF and NCNT/CF were 39.1% and 27.7%, respectively (Fig. S17a-b). When PMS and light were presented concurrently, the degradation efficiencies of PE by Co-NCNT/CF and NCNT/CF reached ~85% and 44%, respectively (Fig. 4a), indicating the excellent performance of Co-NCNT/CF for PMS activation during solar evaporation. Additionally, the rate constant of Co-NCNT/CF+PMS (0.035 min⁻¹) was much higher than that of NCNT/CF+PMS (0.011 min⁻¹) (Fig. 4c, Fig. S17c). However, in the absence of PMS, the evaporators showed a significantly lowered degradation of PE under solar irradiation (1 kW m⁻²) (Fig. S17d). It was found that Co-NCNT/CF exhibited a stable phenol removal performance, and other two types of organic wastewater could be effectively degraded with the addition of Co-NCNT/CF photothermal membrane (Fig. S18). Meanwhile, the Co-NCNT/CF evaporator delivered an evaporation rate of 3.85 kg m⁻² h⁻¹, which was about ~1.1 times and 1.6 times higher than that of NCNT/CF and CF, respectively (Fig. 4b-c). The degradation activities and evaporation rates can be further enhanced by increasing the light intensity (Fig. 4d-f, Fig. S19a). On the one hand, high light intensity promoted the plasmonic excitation of Co NPs, which enhanced the overall activity of the catalyst. On the other hand, the increased light intensity could increase the temperature of the evaporation surfaces, thereby increasing the water molecular kinetic energy. This means that enough water molecules escaped from the evaporation surface to increase the saturated vapor pressure and enhance the evaporation rate [50–52]. During solar-driven evaporation, the surface temperature of the evaporators varied with the light intensities (Fig. 4g, Fig. S20). However, the side surface temperatures of the evaporators were consistently lower than the ambient temperature, confirming that the system could extract energy from the surrounding environment. In addition, the influences of PE and PMS concentrations on PE degradation and evaporation performance were also explored (Fig. 4h-i, Fig. S19b, Fig. S21). As shown in Fig. 4i, the PE concentration showed negligible impact on evaporation performance. Importantly, the Co-NCNT/CF evaporator showed both higher PE degradation and evaporation rate compared to other reported 3D evaporators (Fig. S22).

2.4. Investigation of reactive species and interfacial interactions

Radical quenching experiments and electron spin resonance (ESR) were performed to identify main active species of the Co-NCNT/PMS system during solar evaporation. Methyl alcohol (MeOH), tert-butanol (TBA), Ar and furfuryl alcohol (FFA) are usually considered the scavengers for •OH/SO₄^{•-}, •OH, •O₂ and ¹O₂, respectively [53,54]. Apparently, the degradation efficiencies decreased significantly after the introduction of MeOH and FFA, indicating that both SO₄^{•-} and ¹O₂ were the main active species for PE degradation (Fig. S23a-b). Correspondingly, the contributions of SO₄^{•-} and ¹O₂ were as high as 56.34% and 92.86%, respectively. In contrast, neither •OH nor •O₂ significantly inhibited the degradation of PE. Moreover, ESR (Fig. S23c-d) further manifest that the system can produce SO₄^{•-} and ¹O₂ during solar evaporation, matching well with the results of radical quenching experiments.

The mechanisms underlying the evolution of active species in this system can be summarized as follows. First, Co-NCNT/CF can serve as a platform for the enrichment of both PMS and PE. Second, electron-rich N sites can transfer one electron to PMS and induce its decomposition to release SO₄^{•-} and •OH (Eqs. (1)–(2)). Then, PMS can be oxidized into SO₅^{•-} by donating one electron to electron-deficient C sites, and the resultant SO₅^{•-} may produce ¹O₂ through reacting with water molecules (Eqs. (3)–(4)). The ROS produced by the Co-NCNT/CF@PMS system to degrade pollutants (Eq. (5)).



To unveil the intrinsic mechanism for PMS activation, DFT calculations were further performed to probe the interactions between PMS and CNT. Electrostatic and van der Waals interactions are the two main intermolecular interactions [55]. Firstly, the electrostatic potentials (ESP) distribution is visualized by electron density isosurface. Fig. 5a clearly showed that most regions of the van der Waals surfaces of the CNT exhibited negative electrostatic potentials (ESP), and the areas of the positive and negative parts were calculated to be 242.8 and 574.9 Å², accounting for 70.3% and 29.7% of the entire van der Waals surfaces, respectively. The ESP of van der Waals surface is closely related to the characteristics of intermolecular interactions. Redder areas in the inset indicated more positive ESP, while bluer areas represented more negative ESP. It can be seen that the part where the ESP is negative plays a dominant role. This result indicates that electrons are more easily attracted to the inner-surface of CNT. Furthermore, the van der Waals potential [56] was used to reveal the van der Waals interactions between the CNT and the external environment. Fig. S24 showed that the van der Waals potential was very negative on the inner-surface of CNT, with the most negative value being −3.1 kcal/mol. Consequently, the adsorption capacity on the outer-surface due to van der Waals effect was much lower than that on the inner-surface of CNT. Fig. 5b clearly revealed the distribution characteristics of van der Waals potential. Therefore, it was confirmed that CNT had a tendency to adsorb molecules onto the inner-surface [55].

To further verify this process, the interactions of PMS with the inner and outer surfaces of CNT (i.e., PMS-in-CNT and PMS-out-CNT) were analyzed. The optimized geometry structure is shown in Fig. S25. The properties of π electrons play a significant role in determining various properties of CNT. It can be found that the delocalization extent of π electrons on the inner surface of CNT is clearer (Fig. 5c and Fig. S26), demonstrating the fact that the π electronic density is higher on the inner surface of CNT than that on the outer surface. For PMS-in-CNT (Fig. 5c), the isosurface exists in the PMS, indicating that the PMS also possesses delocalized π electrons. It graphically reveals regions where weak interactions occur. Nevertheless, there is no LOL-π isosurface on the PMS of PMS-out-CNT system. To explore the mechanism on PMS activation, Independent Gradient Model (IGM) and Reduced Density Gradient (RDG) were used to reveal the weak interaction regions and features between CNT and PMS. The color of the atoms in the CNT exhibits atomic contribution to the interactions, that is, the redder the region, the greater the contribution of the atoms. Fig. 5d and Fig. S27 graphically demonstrate the fact that the interaction area between CNT and PMS is larger in PMS-in-CNT compared to PMS-out-CNT. The green isosurface represents the weak interaction region between the CNT and PMS. It can be observed that PMS-in-CNT exhibits more spikes, whereas the PMS-out-CNT possesses the minimum green spikes (Fig. S28), indicating a strong van der Waals interaction between PMS and CNT in PMS-in-CNT. The above results prove that the adsorption and activation of PMS are more effective in the confined space of Co-NCNT system compared to the unconfining system.

The dual descriptor (Fig. S29) further provided the nucleophilic and electrophilic sites of PE. Generally, the atom sites with positive and negative values are more favorable to react with nucleophilic and electrophilic attack, respectively. Additionally, the electron transfer between CNT and PMS was further analyzed by electron density difference. The green and blue regions in Fig. S30 represent the parts where electron density is increased and decreased after the interaction between

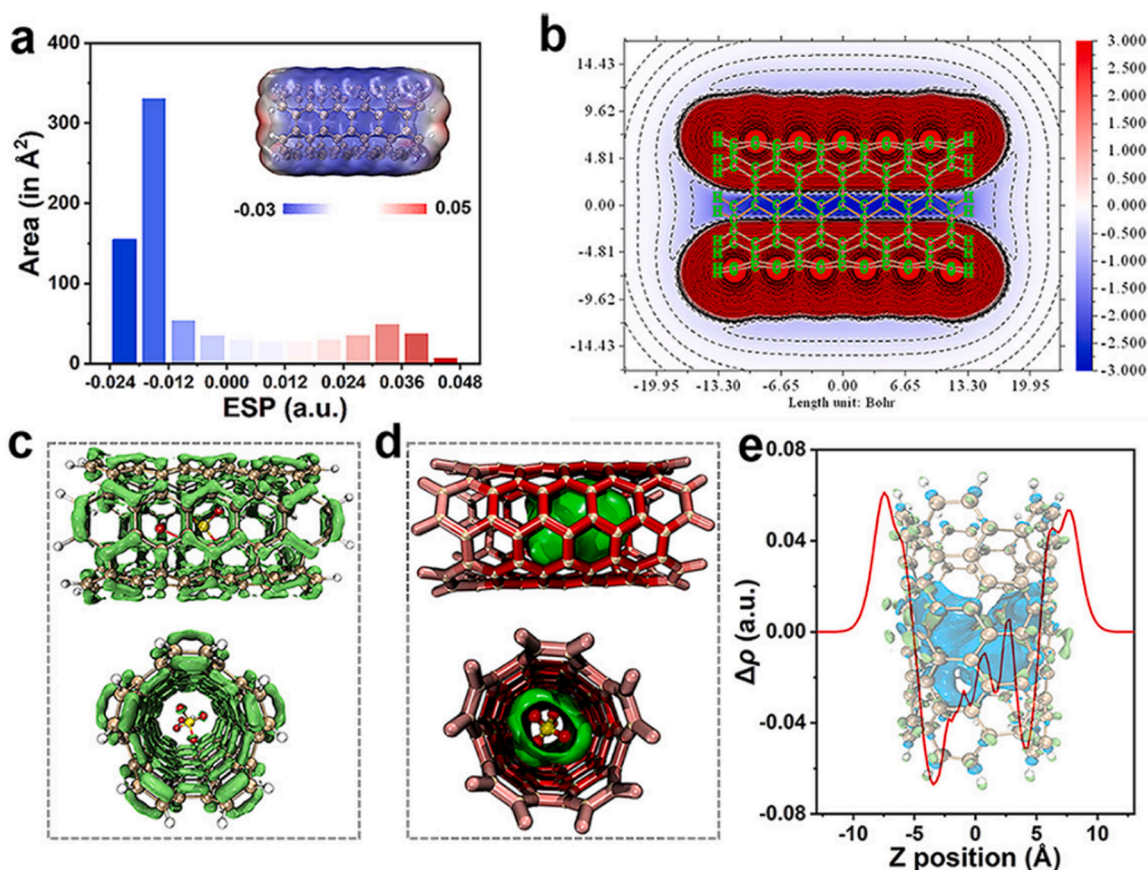


Fig. 5. (a) Area distribution of different ESP intervals. Insert: ESP mapped van der Waals surface (isosurface of $\rho = 0.001$) of the CNT. The color scale is given in a.u. (b) van der Waals potential in a cutting plane of the nanotube fragment. Contour lines of positive and negative parts are in solid and dash styles, respectively. The color scale is in kcal/mol. (c) Isosurface map of LOL- π of PMS-in-CNT. Isovalue of 0.53 is employed. (d) IGM analysis for the PMS-in-CNT complex. Isovalue of 0.006 is employed. (e) Local integral curve and electron density difference of PMS-in-CNT corresponding to $\Delta\rho = \rho(\text{CNT-PMS}) - [\rho(\text{CNT}) + \rho(\text{PMS})]$. Isovalue of 0.00035 is employed.

CNT and PMS. Furthermore, from the electron density difference analysis (Fig. S30a), it can be seen that there is also significant electron transfer between PE and CNT, at which point PE is degraded with the loss of electrons. From the curve with the isosurface graph shown in Fig. 5e and Fig. S30b, the peaks lower and higher than zero correspond to the blue and green isosurfaces. From this curve, the amount of $\Delta\rho$ at each slice can be investigated quantitatively. It can be seen that electron in PMS prone to be significantly transferred to CNT, which is bound to be accompanied by the change in system energy. By calculating the fragment charge, the electron transfer amount from PMS to CNT in the PMS-in-CNT system is 0.494, while the electron transfer amount is only 0.019 in the PMS-out-CNT system. The above results further indicate that the enhanced van der Waals interactions facilitated PMS adsorption and activation on the confined inner-surface of Co-NCNT compared to that in the unconfined system. This result is reminiscent of the prepared Co-NCNT can promote faster PMS activation under light irradiation through the confinement effect, resulting in the generation of active species and the consequent degradation of PE during solar evaporation.

2.5. VOC-intercepting performance

To elucidate the VOC removal ability of photothermal Co-NCNT/CF evaporator, the residue concentration of PE molecules as model VOC in the condensed water was measured. As shown in Fig. 6a-b, after solar evaporation over the Co-NCNT/CF evaporator, the concentration of PE in the condensed water was significantly decreased. It was found that the PE molecules could easily contaminate the condensed water during evaporation in the absence of Co-NCNT/CF evaporator, resulting in high

PE concentration in the condensed water (Fig. 6c). In comparison, PE molecules were effectively intercepted when the solar evaporation was implemented with the Co-NCNT/CF evaporator. The concentration of PE in the collected water (0.16 mg L^{-1}) was far below that in the water source (10 mg L^{-1}), confirming 98% PE removal efficiency (Fig. 6d). In addition, no residual PE could be detected in condensed water when initial PE concentration in water was $< 5 \text{ mg L}^{-1}$. These results confirmed the unique and effective VOC removal during interfacial solar evaporation with Co-NCNT/CF evaporator, which could significantly extend the spectrum of water sources for solar evaporation-based water treatment.

2.6. Desalination and outdoor solar evaporation

Desalination performance of the Co-NCNT/CF evaporator was evaluated by solar evaporation of different concentrated NaCl solution. As presented in Fig. 7a-b, the solar evaporation rate decreased from $3.8 \text{ kg m}^{-2} \text{ h}^{-1}$ for 3.5 wt% NaCl solution to $2.9 \text{ kg m}^{-2} \text{ h}^{-1}$ for 25 wt% NaCl solution. The evaporation rate reduced with the increase in NaCl concentration due to the decreased vapor pressure of the NaCl solution [57–59]. Specifically, when the salt concentration increases, since some of the solute molecules will take up spaces at the surface of the liquid, it will limit the number of solvent molecules at the surface. In this scenario, only the solvent molecules located at the surface can be effectively evaporated, the presence of the solute lowers the number of solvent molecules escaping to air, thus lowering the evaporation rate. Nevertheless, during solar evaporation of NaCl solution, no salt crystals were observed on the top surface of the evaporator, which indicated its

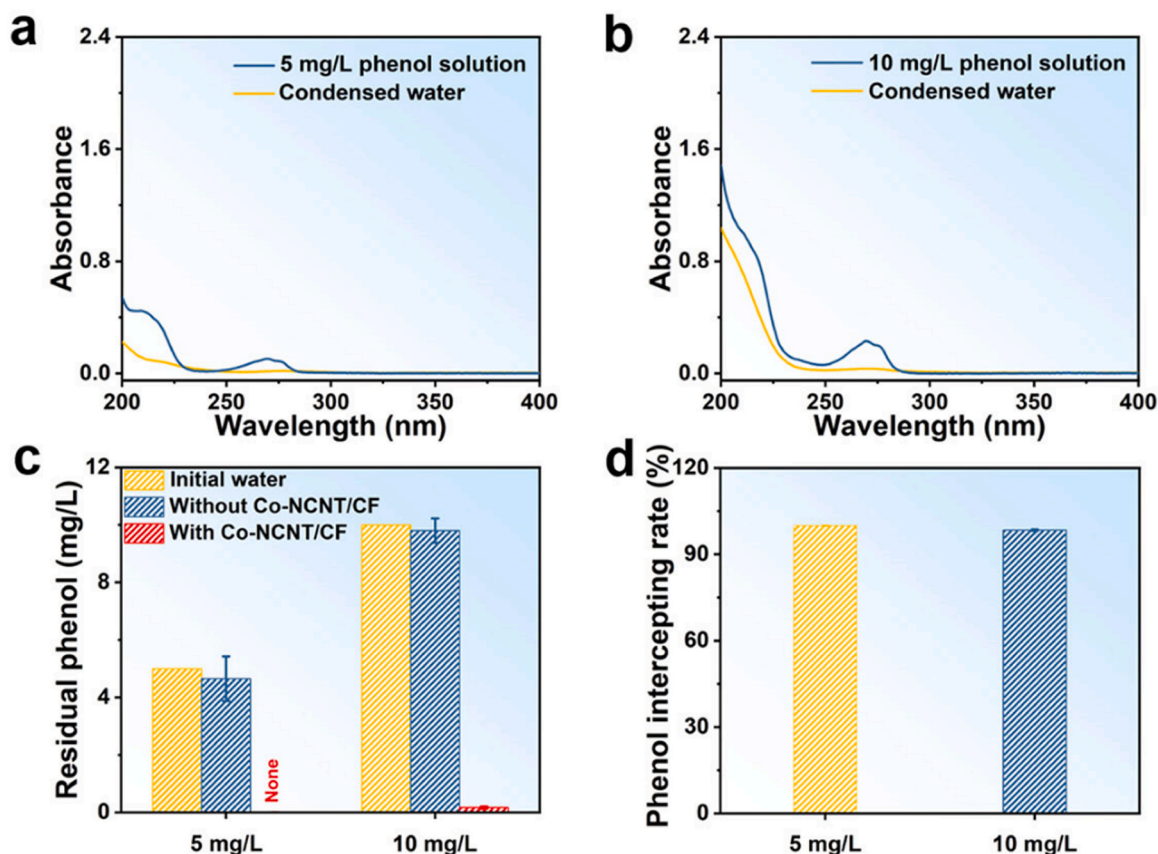


Fig. 6. Absorbance spectra of initial PE solution and condensed water from the vapor generated by Co-NCNT/CF evaporator: (a) 5 mg L⁻¹, (b) 10 mg L⁻¹. (c) Residual PE in condensed water after solar evaporation and (d) the PE intercepting rate of Co-NCNT/CF evaporator towards PE solution with concentration of 5 mg L⁻¹ and 10 mg L⁻¹, respectively.

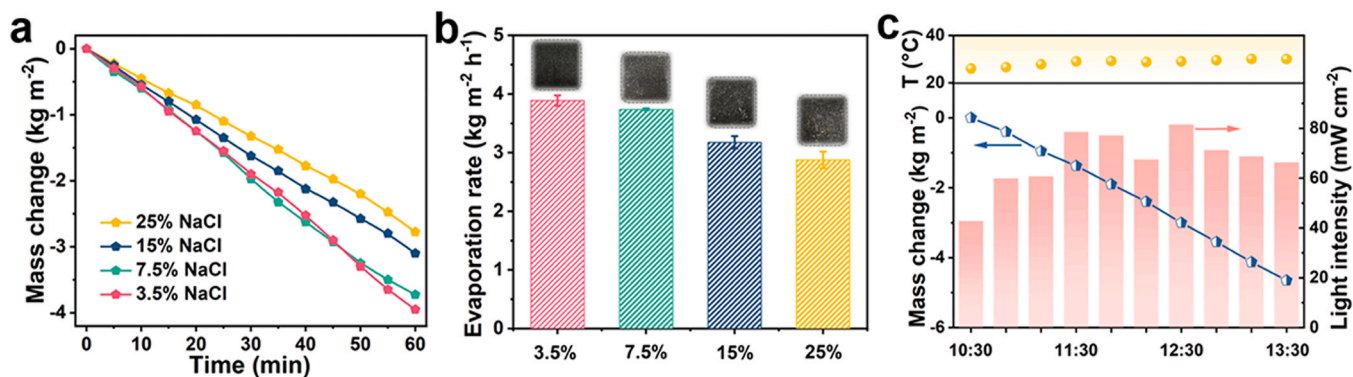


Fig. 7. (a-b) Solar evaporation of NaCl solution with different concentration. (c) Solar evaporation using the Co-NCNT/CF evaporator under natural sunlight irradiation. T: environmental temperature.

excellent salt-rejection capability.

To further verify the solar evaporation under natural sunlight irradiation, an outdoor solar desalination experiment (10:30–13:30, 6 Sep 2022, Nanjing, China) was carried out using a home-made device (Fig. S32). Evaporation conditions including environmental temperature, light intensity and mass change were monitored in real time (Fig. 7c). Under natural sunlight irradiation, vapor was rapidly generated and condensed on the walls of the device. During outdoor tests, although the evaporation rate is varied due to the change of environmental conditions, the Co-NCNT/CF evaporator still exhibited excellent light-to-heat conversion under natural sunlight, with an average water evaporation rate as high as 1.5 kg m⁻² h⁻¹. Therefore, the Co-NCNT/CF

evaporator showed great potential in practical solar-driven desalination in natural environment.

3. Conclusion

In conclusion, a 3D bifunctional Co-NCNT/CF photothermal evaporator with both excellent solar evaporation performance and volatile organic pollutant degradation activity was designed and constructed for versatile water purification. The 3D evaporator with rationally designed evaporation surfaces and evaporator support can significantly increase the evaporation rate by making use of the spontaneously generated internal air convection to facilitate the vapor escape and harvesting extra

energy from the surrounding environment. The evaporator simultaneously achieved highly efficient solar evaporation ($3.85 \text{ kg m}^{-2} \text{ h}^{-1}$) and purification of volatile organic wastewater. DFT calculations showed that the enhanced van der Waals interactions facilitated PMS adsorption and activation on the confined inner surface of Co-NCNT. The results of this study provide new insights into the design of photo-thermal evaporators for clean water production from various water sources containing VOC.

CRedit authorship contribution statement

Lingfang Cui: Methodology, Software, Validation, Visualization, Writing – original draft. **Peifang Wang:** Validation, Visualization, Formal analysis, Writing – review & editing. **Huinan Che:** Validation, Formal analysis. **Xin Gao:** Calculation. **Juan Chen:** Formal analysis. **Bin Liu:** Writing – review & editing, Formal analysis. **Yanhui Ao:** Conceptualization, Writing – review & editing, Supervision, Funding acquisition, Formal analysis.

Declaration of Competing Interest

The authors declare that they have no known competing financial interests or personal relationships that could have appeared to influence the work reported in this paper.

Data Availability

Data will be made available on request.

Acknowledgements

We are grateful for grants from Natural Science Foundation of China (51979081, 52100179), National Science Funds for Creative Research Groups of China (No.51421006), PAPD and Australian Research Council (FT190100485, DP220100583).

Author statement

L. Cui, P. Wang and Y. Ao designed the whole experiments. H. Che contributed to the theoretical calculations. L. Cui, Y. Ao and H. Xu wrote the manuscript. Y. Ao supervised the project. P. Wang, Y. Ao and H. Xu provided constructive suggestions and improved the paper quality by discussions. All authors analysed the experimental results and revised the manuscript.

Appendix A. Supporting information

Supplementary data associated with this article can be found in the online version at [doi:10.1016/j.apcatb.2023.122988](https://doi.org/10.1016/j.apcatb.2023.122988).

References

- [1] Y. Xiao, C. Li, X. Zhou, N. Tao, M. Ye, Removal of typical volatile organic compounds in condensed freshwater by activated persulfate during interfacial solar distillation, *ACS ES&T Water* 1 (11) (2021) 2423–2430.
- [2] Y.D. Wang, X. Wu, T. Gao, Y. Lu, X.F. Yang, G.Y. Chen, G. Owens, H.L. Xu, Same materials, bigger output: A reversibly transformable ^2D – ^3D photothermal evaporator for highly efficient solar steam generation, *Nano Energy* 79 (2021), 105477.
- [3] X.Q. Li, J.L. Li, J.Y. Lu, N. Xu, C.L. Chen, X.Z. Min, B. Zhu, H.X. Li, L. Zhou, S. N. Zhu, T.J. Zhang, J. Zhu, Enhancement of interfacial solar vapor generation by environmental energy, *Joule* 2 (7) (2018) 1331–1338.
- [4] L.B. Zhang, B. Tang, J.B. Wu, R.Y. Li, P. Wang, Hydrophobic light-to-heat conversion membranes with self-healing ability for interfacial solar heating, *Adv. Mater.* 27 (33) (2015) 4889–4894.
- [5] F. Zhao, Y.H. Guo, X.Y. Zhou, W. Shi, G.H. Yu, Materials for solar-powered water evaporation, *Nat. Rev. Mater.* 5 (5) (2020) 388–401.
- [6] G. Ni, G. Li, S.V. Boriskina, H.X. Li, W.L. Yang, T.J. Zhang, G. Chen, Steam generation under one sun enabled by a floating structure with thermal concentration, *Nat. Energy* 1 (2016) 16126.
- [7] P. Tao, G. Ni, C.Y. Song, W. Shang, J.B. Wu, J. Zhu, G. Chen, T. Deng, Solar-driven interfacial evaporation, *Nat. Energy* 3 (12) (2018) 1031–1041.
- [8] L.N. Zhang, Z.Y. Xu, L. Zhao, B. Bhatia, Y. Zhong, S. Gong, E.N. Wang, Passive, high-efficiency thermally-localized solar desalination, *Energy Environ. Sci.* 14 (4) (2021) 1771–1793.
- [9] Y. Wang, X. Wu, P. Wu, J. Zhao, X. Yang, G. Owens, H. Xu, Enhancing solar steam generation using a highly thermally conductive evaporator support, *Sci. Bull.* 66 (24) (2021) 2479–2488.
- [10] F. Zhao, X. Zhou, Y. Shi, X. Qian, M. Alexander, X. Zhao, S. Mendez, R. Yang, L. Qu, G. Yu, Highly efficient solar vapour generation via hierarchically nanostructured gels, *Nat. Nanotechnol.* 13 (6) (2018) 489–495.
- [11] H. Ghasemi, G. Ni, A.M. Marconnet, J. Loomis, S. Yerci, N. Miljkovic, G. Chen, Solar steam generation by heat localization, *Nat. Commun.* 5 (2014) 4449.
- [12] C.T.K. Finnerty, A.K. Menon, K.M. Conway, D. Lee, M. Nelson, J.J. Urban, D. Sedlak, B.X. Mi, Interfacial solar evaporation by a 3D graphene oxide stalk for highly concentrated brine treatment, *Environ. Sci. Technol.* 55 (22) (2021) 15435–15445.
- [13] J.H. Zhou, Y.F. Gu, P.F. Liu, P.F. Wang, L. Miao, J. Liu, A.Y. Wei, X.J. Mu, J.L. Li, J. Zhu, Development and evolution of the system structure for highly efficient solar steam generation from zero to three dimensions, *Adv. Funct. Mater.* 29 (50) (2019), 190325.
- [14] Y. Shi, R.Y. Li, Y. Jin, S.F. Zhuo, L. Shi, J. Chang, S. Hong, K.C. Ng, P. Wang, A 3D photothermal structure toward improved energy efficiency in solar steam generation, *Joule* 2 (6) (2018) 1171–1186.
- [15] Y.D. Wang, X. Wu, X.F. Yang, G. Owens, H.L. Xu, Reversing heat conduction loss: Extracting energy from bulk water to enhance solar steam generation, *Nano Energy* 78 (2020), 105269.
- [16] X. Wu, Z.Q. Wu, Y.D. Wang, T. Gao, Q. Li, H.L. Xu, All-cold evaporation under one sun with zero energy loss by using a heatsink inspired solar evaporator, *Adv. Sci.* 8 (7) (2021) 2002501.
- [17] C.L. Zhang, Y. Shi, L. Shi, H.X. Li, R.Y. Li, S. Hong, S.F. Zhuo, T.J. Zhang, P. Wang, Designing a next generation solar crystallizer for real seawater brine treatment with zero liquid discharge, *Nat. Commun.* 12 (1) (2021) 998.
- [18] Y.H. Guo, C.M. Dundas, X.Y. Zhou, K.P. Johnston, G.H. Yu, Molecular engineering of hydrogels for rapid water disinfection and sustainable solar vapor generation, *Adv. Mater.* 33 (35) (2021) 2102994.
- [19] Y. Geng, W. Sun, P. Ying, Y. Zheng, J. Ding, K. Sun, L. Li, M. Li, Bioinspired fractal design of waste biomass-derived solar–thermal materials for highly efficient solar evaporation, *Adv. Funct. Mater.* 31 (3) (2021) 2007648.
- [20] J.L. Li, X.Y. Wang, Z.H. Lin, N. Xu, X.Q. Li, J. Liang, W. Zhao, R.X. Lin, B. Zhu, G. L. Liu, L. Zhou, S.N. Zhu, J. Zhu, Over $10 \text{ kg m}^{-2} \text{ h}^{-1}$ evaporation rate enabled by a 3D interconnected porous carbon foam, *Joule* 4 (4) (2020) 928–937.
- [21] T.P. Ding, Y. Zhou, W.L. Ong, G.W. Ho, Hybrid solar-driven interfacial evaporation systems: beyond water production towards high solar energy utilization, *Mater. Today* 42 (2021) 178–191.
- [22] C. Song, D. Qi, Y. Han, Y. Xu, H. Xu, S. You, W. Wang, C. Wang, Y. Wei, J. Ma, Volatile-organic-compound-intercepting solar distillation enabled by a photothermal/photocatalytic nanofibrous membrane with dual-scale pores, *Environ. Sci. Technol.* 54 (14) (2020) 9025–9033.
- [23] D. Xie, M. He, X.R. Li, J. Sun, J. Luo, Y. Wu, F. Cheng, Tree-inspired efficient solar evaporation and simultaneous in-situ purification of ultra-highly concentrated mixed volatile organic wastewater, *Nano Energy* 93 (2022), 106802.
- [24] S. Zhou, R.H. He, J.C. Pei, W.P. Liu, Z.H. Huang, X.G. Liu, J. Wang, Self-regulating solar steam generators enable volatile organic compound removal through in situ H_2O_2 generation, *Environ. Sci. Technol.* 56 (14) (2022) 10474–10482.
- [25] Y. Lu, H. Zhang, D. Fan, Z. Chen, X. Yang, Coupling solar-driven photothermal effect into photocatalysis for sustainable water treatment, *J. Hazard. Mater.* 423 (2022), 127128.
- [26] D.Q. Fan, Y. Lu, H. Zhang, H.L. Xu, C.H. Lu, Y.C. Tang, X.F. Yang, Synergy of photocatalysis and photothermal effect in integrated 0D perovskite oxide/2D MXene heterostructures for simultaneous water purification and solar steam generation, *Appl. Catal. B Environ.* 295 (2021), 120285.
- [27] Y. Lu, D. Fan, Z. Shen, H. Zhang, H. Xu, X. Yang, Design and performance boost of a MOF-functionalized-wood solar evaporator through tuning the hydrogen-bonding interactions, *Nano Energy* 95 (2022), 107016.
- [28] H.N. Che, P.F. Wang, J. Chen, X. Gao, B. Liu, Y.H. Ao, Rational design of donor-acceptor conjugated polymers with high performance on peroxydisulfate activation for pollutants degradation, *Appl. Catal. B Environ.* 316 (5) (2022), 121611.
- [29] P.P. He, H.Y. Bai, Z.F. Fan, L. Hao, N. Liu, B.Y. Chen, R. Niu, J. Gong, Controllable synthesis of N/Co-doped carbon from metal-organic frameworks for integrated solar vapor generation and advanced oxidation processes, *J. Mater. Chem. A* 10 (25) (2022) 13378–13392.
- [30] W. Ren, C. Cheng, P. Shao, X. Luo, H. Zhang, S. Wang, X. Duan, Origins of electron-transfer regime in persulfate-based nonradical oxidation processes, *Environ. Sci. Technol.* 56 (2021) 78–97.
- [31] P.X. Wang, X. He, W. Zhang, J. Ma, J. Jiang, Z.S. Huang, H.J. Cheng, S.Y. Pang, Y. Zhou, X.D. Zhai, Highly efficient removal of p-arsanilic acid with Fe(II)/peroxydisulfate under near-neutral conditions, *Water Res.* 177 (2020), 115752.
- [32] J.B. Chen, X.F. Zhou, P.Z. Sun, Y.L. Zhang, C.H. Huang, Complexation enhances Cu (II)-activated peroxydisulfate: A novel activation mechanism and Cu(III) contribution, *Environ. Sci. Technol.* 53 (20) (2019) 11774–11782.
- [33] C. Marinescu, M. Ben Ali, A. Hamdi, Y. Cherifi, A. Barras, Y. Coffinier, S. Somacescu, V. Raditoiu, S. Szunerits, R. Boukherroub, Cobalt phthalocyanine-supported reduced graphene oxide: A highly efficient catalyst for heterogeneous activation of peroxymonosulfate for rhodamine B and pentachlorophenol degradation, *Chem. Eng. J.* 336 (2018) 465–475.

- [34] Y.X. Zhang, H. Zhang, T. Xiong, H. Qu, J.J. Koh, D.K. Nandakumar, J. Wang, S. C. Tan, Manipulating unidirectional fluid transportation to drive sustainable solar water extraction and brine-drenching induced energy generation, *Energy Environ. Sci.* 13 (12) (2020) 4891–4902.
- [35] T.P. Ding, G.W. Ho, Using the sun to co-generate electricity and freshwater, *Joule* 5 (7) (2021) 1639–1641.
- [36] W.J. Zang, A. Sumboja, Y.Y. Ma, H. Zhang, Y. Wu, S.S. Wu, H.J. Wu, Z.L. Liu, C. Guan, J. Wang, S.J. Pennycook, Single Co atoms anchored in porous N-doped carbon for efficient zinc-air battery cathodes, *ACS Catal.* 8 (10) (2018) 8961–8969.
- [37] H.C. Liu, G.C. Huang, R. Wang, L. Huang, H.Z. Wang, Y.Z. Hu, G.T. Cong, F. Bao, M. Xu, C.Z. Zhu, J. Xu, M.W. Ji, Carbon nanotubes grown on the carbon fibers to enhance the photothermal conversion toward solar-driven applications, *ACS Appl. Mater. Interfaces* 14 (28) (2022) 32404–32411.
- [38] J. Wang, D.F. Gao, G.X. Wang, S. Miao, H.H. Wu, J.Y. Li, X.H. Bao, Cobalt nanoparticles encapsulated in nitrogen-doped carbon as a bifunctional catalyst for water electrolysis, *J. Mater. Chem. A* 2 (47) (2014) 20067–20074.
- [39] H.M. Zhang, C.Y. Hu, M.W. Ji, M.J. Wang, J.L. Yu, H.C. Liu, C.Z. Zhu, J. Xu, Co/Co₉S₈@carbon nanotubes on a carbon sheet: facile controlled synthesis, and application to electrocatalysis in oxygen reduction/oxygen evolution reactions, and to a rechargeable Zn-air battery, *Inorg. Chem. Front.* 8 (2) (2021) 368–375.
- [40] M. Zeng, Y. Liu, F. Zhao, K. Nie, N. Han, X. Wang, W. Huang, X. Song, J. Zhong, Y. Li, Metallic cobalt nanoparticles encapsulated in nitrogen-enriched graphene shells: Its bifunctional electrocatalysis and application in zinc-air batteries, *Adv. Funct. Mater.* 26 (24) (2016) 4397–4404.
- [41] T. Sharifi, F. Nitze, H.R. Barzegar, C.W. Tai, M. Mazurkiewicz, A. Malolepszy, L. Stobinski, T. Wagberg, Nitrogen doped multi walled carbon nanotubes produced by CVD-correlating XPS and Raman spectroscopy for the study of nitrogen inclusion, *Carbon* 50 (10) (2012) 3535–3541.
- [42] X. Li, A.E. Surkus, J. Rabeah, M. Anwar, S. Dastagir, H. Junge, A. Bruckner, M. Beller, Cobalt single-atom catalysts with high atability for selective dehydrogenation of formic acid, *Angew. Chem. Int. Ed.* 59 (37) (2020) 15849–15854.
- [43] N. Zafar, S.N. Yun, M.L. Sun, J. Shi, A. Arshad, Y.W. Zhang, Z.B. Wu, Cobalt-based incorporated metals in metal-organic framework-derived nitrogen-doped carbon as a robust catalyst for triiodide reduction in photovoltaics, *ACS Catal.* 11 (21) (2021) 13680–13695.
- [44] G.L. Wang, S. Chen, X. Quan, H.T. Yu, Y.B. Zhang, Enhanced activation of peroxymonosulfate by nitrogen doped porous carbon for effective removal of organic pollutants, *Carbon* 115 (2017) 730–739.
- [45] K. Feng, S. Wang, D. Zhang, L. Wang, Y. Yu, K. Feng, Z. Li, Z. Zhu, C. Li, M. Cai, Z. Wu, N. Kong, B. Yan, J. Zhong, X. Zhang, G.A. Ozin, L. He, Cobalt plasmonic superstructures enable almost 100% broadband photon efficient CO₂ photocatalysis, *Adv. Mater.* 32 (24) (2020) 2000014.
- [46] P.P. He, L. Hao, N. Liu, H.Y. Bai, R. Niu, J. Gong, Controllable synthesis of sea urchin-like carbon from metal-organic frameworks for advanced solar vapor generators, *Chem. Eng. J.* 423 (2021), 130268.
- [47] C. Gao, J. Zhu, Z. Bai, Z. Lin, J. Guo, Novel ramie fabric-based draping evaporator for tunable water supply and highly efficient solar desalination, *ACS Appl. Mater. Interfaces* 13 (6) (2021) 7200–7207.
- [48] W.X. Chao, X.H. Sun, Y.D. Li, G.L. Cao, R.P. Wang, C.Y. Wang, S.H. Ho, Enhanced directional seawater desalination using a structure-guided wood aerogel, *ACS Appl. Mater. Interfaces* 12 (19) (2020) 22387–22397.
- [49] Y.D. Wang, X. Wu, B. Shao, X.F. Yang, G. Owens, H.L. Xu, Boosting solar steam generation by structure enhanced energy management, *Sci. Bull.* 65 (16) (2020) 1380–1388.
- [50] F.P. Chinard, Colligative properties, *J. Chem. Educ.* 32 (7) (1955) 377.
- [51] F. Rioux, Colligative properties, *J. Chem. Educ.* 50 (7) (1973) 490.
- [52] F.C. Andrews, Colligative properties of simple solutions: solutes simply dilute the solvent; they do not cause tension in the solvent, *Science* 194 (4265) (1976) 567–571.
- [53] X. Gao, J. Chen, H.N. Che, Y.H. Ao, P.F. Wang, Rationally constructing of a novel composite photocatalyst with multi charge transfer channels for highly efficient sulfamethoxazole elimination: mechanism, degradation pathway and DFT calculation, *Chem. Eng. J.* 426 (2021), 131585.
- [54] S.Y. Dong, Y.L. Zhao, J.Y. Yang, X.D. Liu, W. Li, L.Y. Zhang, Y.H. Wu, J.H. Sun, J. L. Feng, Y.F. Zhu, Visible-light responsive PDI/rGO composite film for the photothermal catalytic degradation of antibiotic wastewater and interfacial water evaporation, *Appl. Catal. B Environ.* 291 (15) (2021), 120127.
- [55] T. Lu, Q.X. Chen, van der Waals potential: an important complement to molecular electrostatic potential in studying intermolecular interactions, *J. Mol. Model.* 26 (11) (2020) 315.
- [56] T. Lu, F.W. Chen, Quantitative analysis of molecular surface based on improved Marching Tetrahedra algorithm, *J. Mol. Graph. Model* 38 (2012) 314–323.
- [57] X. Chen, S.M. He, M.M. Falinski, Y.X. Wang, T. Li, S.X. Zheng, D.Y. Sun, J.Q. Dai, Y. H. Bian, X.B. Zhu, J.Y. Jiang, L.B. Hu, Z.J. Ren, Sustainable off-grid desalination of hypersaline waters using Janus wood evaporators, *Energy Environ. Sci.* 14 (10) (2021) 5347–5357.
- [58] M.M. Zou, Y. Zhang, Z.R. Cai, C.X. Li, Z.Y. Sun, C.L. Yu, Z.C. Dong, L. Wu, Y. L. Song, 3D printing a biomimetic bridge-arch solar evaporator for eliminating salt accumulation with desalination and agricultural applications, *Adv. Mater.* 33 (34) (2021) 2102443.
- [59] L.N. Zhang, X.Y. Li, Y. Zhong, A. Leroy, Z.Y. Xu, L. Zhao, E.N. Wang, Highly efficient and salt rejecting solar evaporation via a wick-free confined water layer, *Nat. Commun.* 13 (1) (2022) 849.